Chinese Physics B

Cascade of low-energy surface phonon modes on the B-terminated EuB_6 surface

To cite this article before publication: Yumeng Li *et al* 2026 *Chinese Phys. B* in press https://doi.org/10.1088/1674-1056/ae6568

Cascade of low-energy surface phonon modes on the B-terminated EuB_6 surface

Yumeng Li(李雨萌) [1,2#], Meng Li(李萌) [1,2#], Lijing Huang(黄丽静) [1,2#], Haitao Yang(杨海涛)[1,2,3], Hongqin Xiao(肖洪钦)[1,2], Yuxuan He(何昱萱)[1,2], Geng Li(李更)[1,2,3*], & Hong-Jun Gao(高鸿钧)[1,2,3]

[1] *Beijing National Center for Condensed Matter Physics and Institute of Physics, Chinese Academy of Sciences, Beijing 100190, China*

[2] *School of Physical Sciences, University of Chinese Academy of Sciences, Beijing 100190, PR China*

[3] *Hefei National Laboratory, Hefei 230088, China*

EuB_6 has emerged as a leading candidate magnetic Weyl semimetal, in which spontaneous ferromagnetic order breaks time-reversal symmetry and drives a topological phase transition accompanied by band inversion. Optical studies have extensively investigated the phonon modes associated with the B_6 octahedra, whose internal vibrations play an important role in understanding the physical properties of EuB_6. However, the low-energy phonon modes and their coupling to electrons remain largely unexplored. Here we report a cascade of low-energy phonon modes resolved on the B-terminated surface of EuB_6 prepared by low-temperature *in situ* cleavage. We show that defects significantly modulate the local electron-phonon coupling (EPC) strength. Moreover, a defect-pinned $\sqrt{2}\times\sqrt{2}$ short-range order emerges on the B-terminated surface, which selectively modulates the local density of states (LDOS) and the EPC strength. Our results provide insight into the interplay between low-energy surface phonons, defects, and electron–phonon coupling on the B-terminated surface of EuB_6.

Keywords: EuB_6, inelastic electron tunneling spectroscopy, surface phonons, electron-phonon coupling, short-range order

PACS: 68.35.B-, 68.35.Ja, 63.20.kd, 68.37.Ef, 64.60.Cn

[#]These authors contributed equally to this work.

[*]Correspondence to: gengli.iop@iphy.ac.cn.

In low-carrier systems with localized magnetic moments, the energy scales of spin excitations and lattice vibrations are often comparable and can strongly influence charge dynamics.[1-5] Such interplay has been invoked to explain emergent phenomena including magnetic polaron formation[6-9]. A representative materials family is RB_6 (R = Sm, Eu, Yb and Ce.), which host diverse electronic ground states ranging from mixed-valence Kondo insulators to low-carrier ferromagnets.[10-12] Their (001) surfaces are strongly polar and exhibit a charge discontinuity,[13,14] often resulting in coexisting rare-earth-terminated and B-terminated domains together with surface charge compensation.[14-16] This complexity makes it challenging to directly relate a given surface structure to its low-energy spectral response. Within this family, optical probes such as Raman and infrared spectroscopy have been widely used to assign the symmetry and energy of Γ-point optical phonons.[17,18] In several RB_6 compounds, spectral anomalies associated with magnetic order or magnetic scattering channels have been reported, suggesting coupling among spin, lattice, and charge degrees of freedom.[7,8,17,19,20] However, these optical probes are constrained by the long-wavelength limit and selection rules, full phonon-branch coverage and local-environment-dependent coupling variations are therefore often inaccessible.[21,22]

As a prototypical low-carrier ferromagnet in the RB_6 family, EuB_6 has been extensively studied by transport and optical probes.[8,9,17,23-29] Near the Curie temperature, a macroscopic picture has emerged involving ferromagnetic order,[17,26,30] colossal magnetoresistance,[9,31] and magnetic-polaron-related[6-8] behavior. These studies suggest that coupling between lattice and spin degrees of freedom near the critical point can influence low-energy electrons.[31] Consistently, Raman and infrared spectroscopy on EuB_6 have identified several Γ-point optical phonon modes and their symmetry indicators, and modifications of optical line shapes associated with magnetic correlations have also been reported.[7,17] Nevertheless, experimental evidence for lower-energy vibrational channels, particularly those away from the Γ point or sensitive to local environments, remains limited. By contrast, inelastic electron tunneling spectroscopy (IETS) can resolve features associated with local electron-vibration coupling.[5] It can provide complementary clues for low-energy vibrations that are invisible in, or difficult to separate by, optical spectra.

In this work, scanning tunneling microscopy/spectroscopy (STM/S) and IETS are performed on the B-terminated surface of EuB_6 after *in situ* cleavage at low temperature. On the B-terminated surface, a cascade of inelastic channels is resolved at approximately 11, 31, 55, and 93 mV. While the ~93 meV feature matches the energy scale of the T_{2g} shear Raman mode of the B_6 octahedra,[7,32] the remaining low-energy modes cannot be straightforwardly assigned to previously reported Raman-active phonons, suggesting additional surface phonon modes. Near defects, the low-energy electronic states around the Fermi level are markedly enhanced, whereas the energies of these inelastic channels remain nearly

unchanged and their excitation probabilities are redistributed in a mode-selective manner. This behavior indicates that defects modulate the local electron–phonon coupling strength without shifting the mode energies. Furthermore, Fourier analysis reveals a $\sqrt{2}\times\sqrt{2}R45°$ short-range order with a finite correlation length near defects, suggesting that the B-terminated surface may achieve local charge compensation and structural reorganization through defect pinning.

EuB_6 crystallizes in the a CaB_6-type simple-cubic structure (space group $Pm\bar{3}m$; Fig. 1(a)). B atoms form B_6^{2-} octahedra connected by inter-octahedral B-B bonds, while Eu^{2+} ions donate electrons to the boron framework, giving the material a mixed ionic-covalent character. The (001) surface is strongly polar because oppositely charged layers stack alternately along the surface normal.[33,34] Consequently, cleavage often produces surfaces with different terminations and varying degrees of surface reconstruction.

Single crystals of EuB_6 were grown using the Al-flux method.[25] Starting materials with a molar ratio of Eu:B:Al = 1:8:100 were loaded into an alumina crucible and heat to 1773 K under high-purity Ar. Then, the furnace was slowly cooled to 1573 K at 2 K/h before cooling to room temperature. The obtained crystals were washed with NaOH solution and deionized water, yielding black cubic crystals. STM measurements were performed in a home-built system with a base pressure below 1×10^{-10} mbar at the temperature of 4.2 K.[35] Electrochemically etched tungsten tips were used in constant-current mode with the bias voltage applied to the sample. STS and IETS were acquired using a lock-in technique with a modulation amplitude of 10 mV at 971 Hz.

After low-temperature *in situ* cleavage of EuB_6, two stable surfaces are reproducibly observed in STM images. One surface shows square atomic lattice and disordered corrugations (Supplement Information Fig. 1(a)), and is assigned to the Eu-terminated surface. The relatively weak surface binding of Eu atoms can lead to aggregation or disorder after cleavage.[10] An ordered region of the Eu terminated surface is shown in Fig. 1(b), where abundant defects are visible and appear as dark spots. The other surface is comparatively flat and is assigned to the B-terminated surface (Fig. 1(d)). Both terminated surfaces exhibited a regular square lattice (Fig. 1(c),(e)) with a lattice constant of ~4.14 Å, consistent with previous reports.[24] A high density of defects is observed on the B-terminated surface. Most defects show fourfold symmetry, while long-range lattice order remained preserved around them. The spectroscopic measurements and defect analyses discussed below focus on the B-terminated surface.

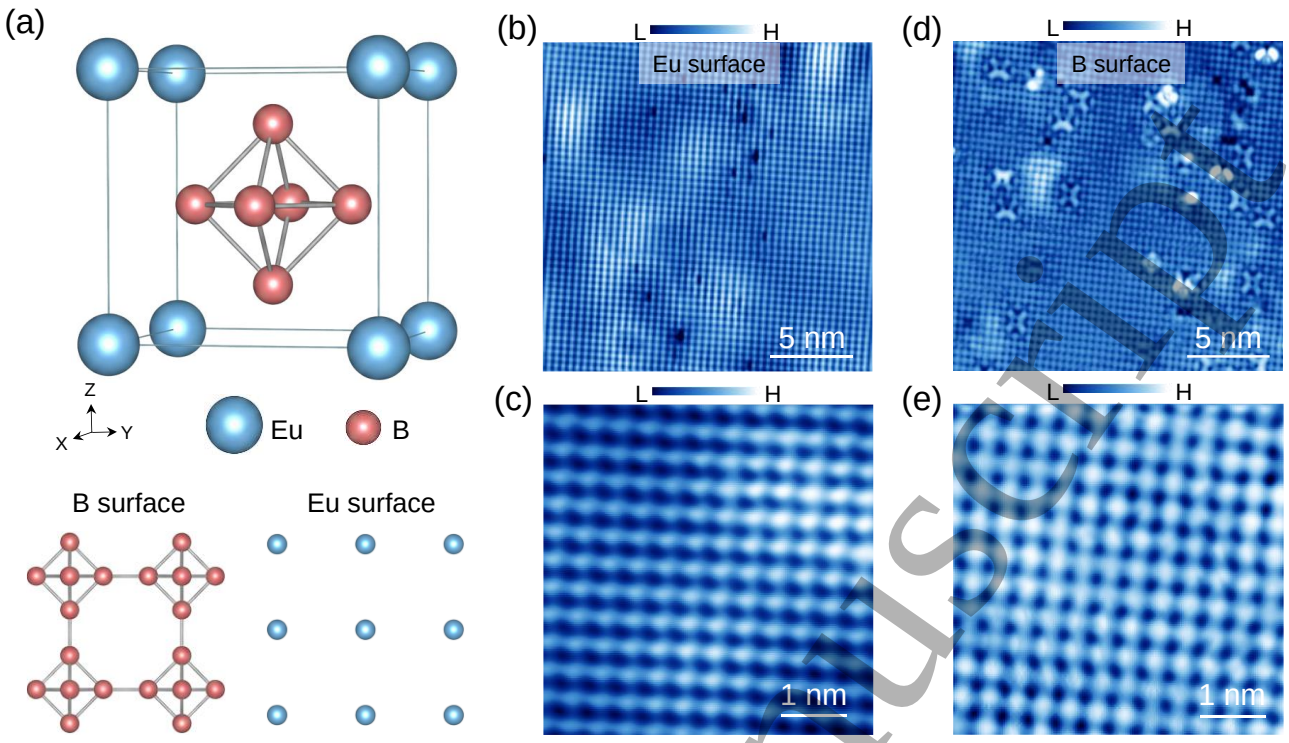

Fig. 1. Crystal structure of EuB_6 and STM images of the two terminating surfaces. (a), Schematic of the CaB_6-type simple cubic structure of EuB_6, consisting of a simple cubic Eu sublattice and a network of B_6 octahedra at the body-center positions. (b), STM image (V_s =-200 mV, I_t =200 pA) of the Eu-terminated surface. (c), Zoom-in STM image (V_s =-200 mV, I_t =60 pA) of (b). (d), STM image (V_s =-100 mV, I_t =200 pA) of the B-terminated surface. (e), Zoom-in STM image (V_s =-100 mV, I_t =60 pA) of (d).

A wide-energy-range dI/dV spectrum is acquired on an intact lattice area of the B-terminated surface far from defects (Fig. 2(a),(b)). The local density of states (LDOS) is higher in the valence band and exhibits a subtle kink near -0.4 V, while remaining very low above -0.2 V. By contrast, spectra taken on the Eu-terminated surface show the opposite trend, with a higher LDOS in the conduction band (Supplement Information Fig. 1(b),(c)), indicating that the two terminated surfaces contribute differently to the low-energy electronic structure. Consistent with previous studies, the valence-band states near the Fermi energy (E_F) mainly derive from B-2p orbitals, whereas the conduction-band states originate primarily from Eu-5d orbitals.[24,36,37]

Bias-dependent STM images of the B-terminated surface (Supplement Information Fig. 2(a)-(d)) further reveal that the spatial inhomogeneity around defects becomes more pronounced near -0.2 V and is relatively uniform at other biases. Previous angle-resolved photoemission spectroscopy (ARPES) studies reported that two low-energy subbands, α_2 (hole-like) and β_1 (electron-like), are nearly

degenerate near -0.2 V.[37] A defect-induced local potential may therefore modify their relative spectral weight, leading to the observed bias-dependent contrast. Wide-energy-range dI/dV spectra show no resolvable dependence on either in-plane or out-of-plane magnetic fields (Supplement Information Fig. 3(a),(b)).

To examine the low-energy excitations in more detail, dI/dV spectra were acquired in a narrow energy window around E_F (Fig. 2(c)). The spectrum displays an approximately V-shaped background with multiple step-like features that appear nearly symmetrically about zero bias. A dI/dV linecut taken along the dashed line in Fig. 2(a) shows that these kinks occur at nearly fixed energies over several nanometers, with only their intensities varying spatially (Fig. 2(d),(e)). This behavior suggests the presence of a cascade of inelastic channels.

The corresponding d^2I/dV^2 spectrum at zero magnetic field (Fig. 2(h)) reveals a series of peak-dip structures characteristic of inelastic tunneling. The peak positions at positive bias are 11.4 ± 0.1 mV, 30.6 ± 0.1 mV, 55.0 ± 0.2 mV, and 92.1 ± 0.3 mV, with corresponding dips at negative bias, giving approximately symmetric features at -11.0 ± 0.3 mV, -31.2 ± 0.2 mV, -54.3 ± 0.2 mV, and -93.4 ± 0.6 mV. For consistency, the positive-bias peaks are used to define the energies of the inelastic channels. Each feature exhibits an asymmetric peak-dip line shape arising from interference between elastic and inelastic tunneling processes within the junction. [38]

Compared with reported Raman modes, the 93 meV mode matches the T_{2g} shear vibration of the B_6 octahedra.[7,32] The remaining lower-energy modes, however, lack one-to-one correspondence with previously reported Raman-active phonons. A spatially resolved d^2I/dV^2 linecut (Fig. 2(f),(g)) confirms that the four inelastic channels remain at fixed energies while their intensities vary periodically in space. Furthermore, measurements performed under out-of-plane magnetic fields of B_z = 2 T, 4 T, and 6 T show no measurable shift in the inelastic channel energies (Fig. 2(h)). This field independence indicates that the observed inelastic channels originate from phonon excitations. It is worth noting that, as shown in the upper panel of Fig. 2h, the dI/dV background near E_F also changes under finite magnetic fields. This is consistent with the change in the LDOS induced by the spin-canting process and the ensuing topological phase transition as the magnetic field is increased along the [001] direction.[37] Therefore, the difference in IETS intensity between 0 T and finite fields more likely reflects the influence of the field-modulated low-energy electronic background on the spectral weight of the inelastic signals.

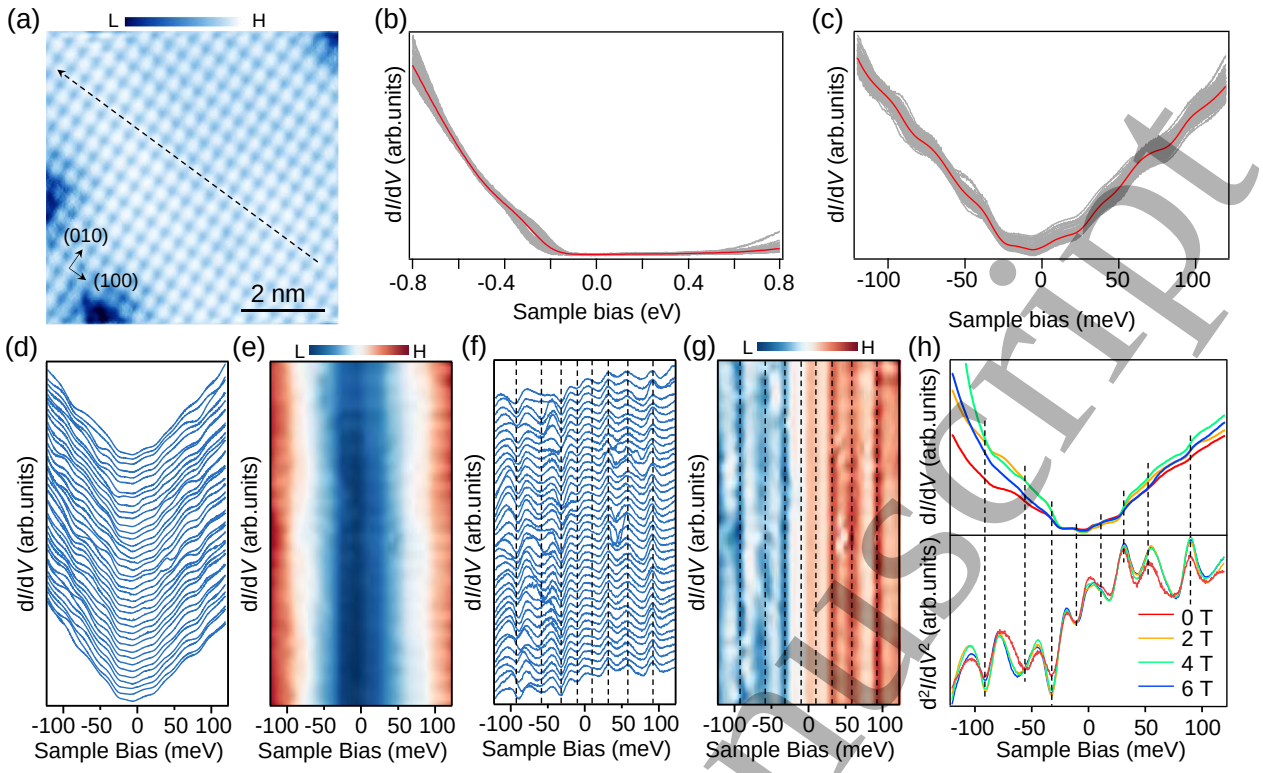

Fig. 2. Electronic properties and inelastic tunneling features on the B-terminated surface. (a), STM image (V_s =-100 V, I_t =600 pA) of the B-terminated surface. (b), Averaged dI/dV spectrum in a wide energy range. (c), Averaged dI/dV spectrum in a narrow energy range around the Fermi level. (d),(e), dI/dV waterfall plot (d) and intensity map (e) of the linecut taken along the black dash line in (a). (f),(g), d^2I/dV^2 waterfall plot (f) and intensity map (g) of the linecut taken along the black dash line in (a). The dashed lines mark the energy positions of symmetric peak-dip pairs in IETS. (h), Top: comparison of dI/dV spectra at zero field and under different applied magnetic fields; bottom: comparison of d^2I/dV^2 spectra at zero field and under magnetic fields of 2 T, 4 T, and 6 T. Dashed lines mark the energy positions of symmetric peak-dip pairs in IETS.

Atomic-resolution STM images reveal several representative defects on the B-terminated surface (Fig. 3(a)). Because the covalent B_6 octahedral network does not provide a natural cleavage plane, cleavage may occur either between neighboring octahedra, producing relatively regular surfaces, or by breaking B-B bonds within the octahedra, generating defects in the topmost or subsurface layers.[15,39] Based on their apparent symmetry and contrast in STM images, the observed defects can be classified into four types: type I (checkerboard; Fig. 3(b)), type II (X-shaped; Fig. 3(c)), type III (bright cross; Fig. 3(d)), and type IV (petal-like; Fig. 3(e)). Except for type I, the dominant elongation of type II-IV defects occurs along the (110) direction. This trend is likely associated with anisotropic relaxation or bond

rearrangement in the surface or subsurface layers after B-B bond rupture in the B_6 octahedra. For type II-IV defects, the central B site (at the centers of the dashed orange squares in Fig. 3(c)-(e)) appears markedly darker than the surrounding lattice, indicating that the defect strongly perturbs its nearest-neighbor atoms.[39]

To examine their electronic influence, a representative type-I defect was selected for spectroscopic measurements. dI/dV spectra acquired near the defect exhibit a shallower V-shaped profile compared with spectra obtained on intact lattice regions (Fig. 3(f)), indicating an enhancement of the LDOS, similar to behavior reported near defects in SmB_6.[39] A linecut across the defect further shows that the LDOS enhancement is largely confined to a single lattice site adjacent to the defect and decays rapidly with distance (Fig. 3(g)), indicating a short-range charge-density modulation on the lattice length scale. Bias-dependent dI/dV maps obtained in regions containing multiple defect types reproducibly show similar local enhancement patterns (Supplementary Fig. 4), suggesting that this behavior is a general feature of the defect landscape rather than an isolated case. These observations indicate that disruption of B-2p dangling bonds and local reconstruction of the B_6 octahedra modify the local potential landscape and hybridization conditions of the surface states.[36] Despite these strong local electronic effects, the peak energies of the inelastic channels remain unchanged near defects, whereas the spectral intensities of the ~31 mV and ~55 mV phonon modes are suppressed. This indicates that defects primarily modulate the local electron-phonon coupling (EPC) strength rather than altering the phonon energies.

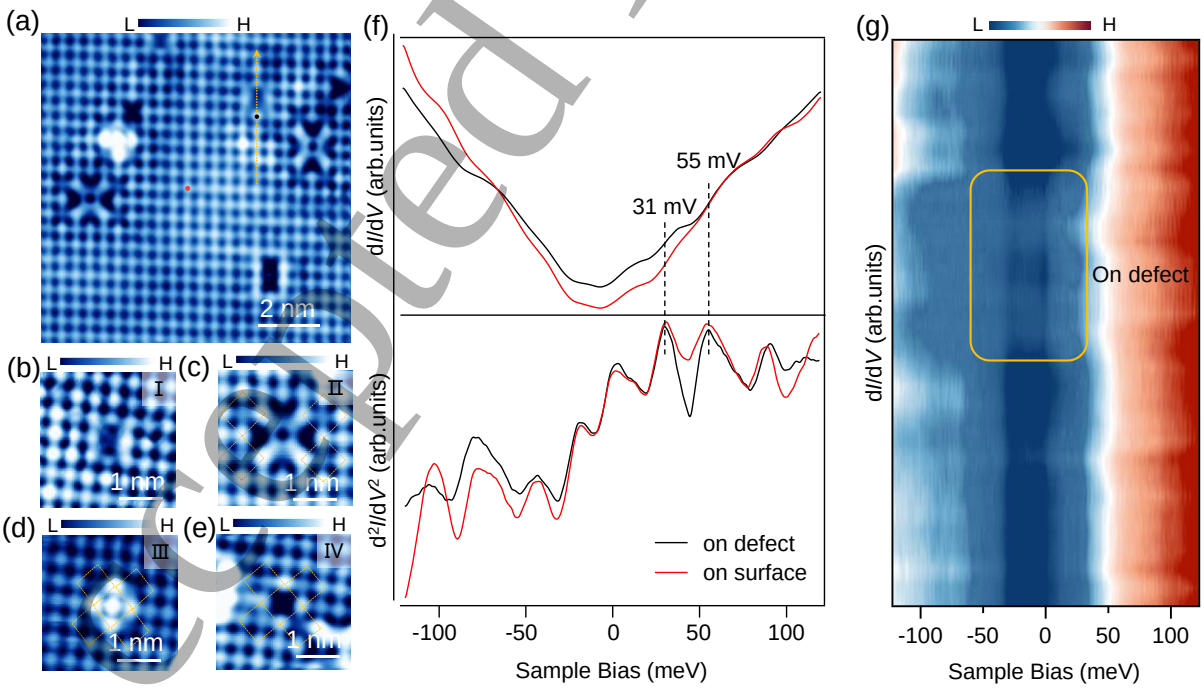

Fig. 3. Defect-induced modulation of low-energy electronic states and IETS. (a), STM image (V_s =-120 mV, I_t =1 nA) of the B-terminated surface containing several defects. (b)-(f) Defects on the B-terminated surface (V_s =-100 mV, I_t =600 pA) are classified according to their local appearance into four types: type I (checkerboard; (b)), type II (X-shaped; (c)), type III (bright cross; (d)), and type IV (petal-like; (e)). The central B sites within the orange dashed squares appear darker than the surrounding sites. (f), Comparison of dI/dV (top) and d^2I/dV^2 (bottom) spectra acquired at the atom adjacent to a defect (black dot in (a)) and at a remote site in the intact lattice (red dot in (a)). Dashed lines mark the peak positions at 31 mV and 55 mV. (g), dI/dV linecut intensity map taken along the orange dashed line across the defect in (a).

To further examine this effect, normalized IETS (N-IETS) maps, defined as (d^2I/dV^2)/(dI/dV), are acquired in defect-rich regions at biases corresponding to the defect-sensitive phonon modes (Fig. 4(a)-(c)). Compared with conventional d^2I/dV^2, N-IETS suppresses variations arising from LDOS changes and more directly reflects the strength of electron-vibration coupling.[5,40-42] In the N-IETS maps at 33 mV and 55 mV, the inelastic signal is spatially inhomogeneous, indicating that the EPC strength is redistributed by the local environment. The signal is suppressed at defect centers and exhibits an anisotropic texture that follows the defect shape. One possible mechanism is that the local symmetry lowering introduced by the short-range modulation alters the selection rules and visibility of inelastic processes[43], whereas local bond rearrangement near defects can renormalize vibrational states through changes in force constants.[32,44] Together, these effects can produce mode-selective enhancement of the EPC.

We next examine the influence of defects on the surrounding electronic structures. Large-area STM images of the B-terminated EuB_6 surface reveal a high density of defects (Fig. 4(d), red box). Corresponding Fourier transform image reveals, in addition to the Bragg peaks (Fig. 4(e), blue circles), a new order near the M points at (±1/2, ±1/2) (Fig. 4(e), red circles),[45] corresponding to a $\sqrt{2}\times\sqrt{2}$ R45° modulation. An inverse Fourier transform of this signal reveals that the $\sqrt{2}\times\sqrt{2}$ modulation is localized around individual defects and decays over ~4-5 lattice constants (Fig. 4(f)). The $\sqrt{2}\times\sqrt{2}$ modulation can be reproducibly observed on the B-terminated surface of different EuB_6 samples and therefore shows a degree of universality. These observations indicate that the $\sqrt{2}\times\sqrt{2}$ short-range order is pinned by defects and produces a local lattice modulation that selectively modifies the near-neighbor LDOS and the local EPC strength. This defect-pinned lattice modulation naturally explains the spatial redistribution of the phonon-related inelastic signals.

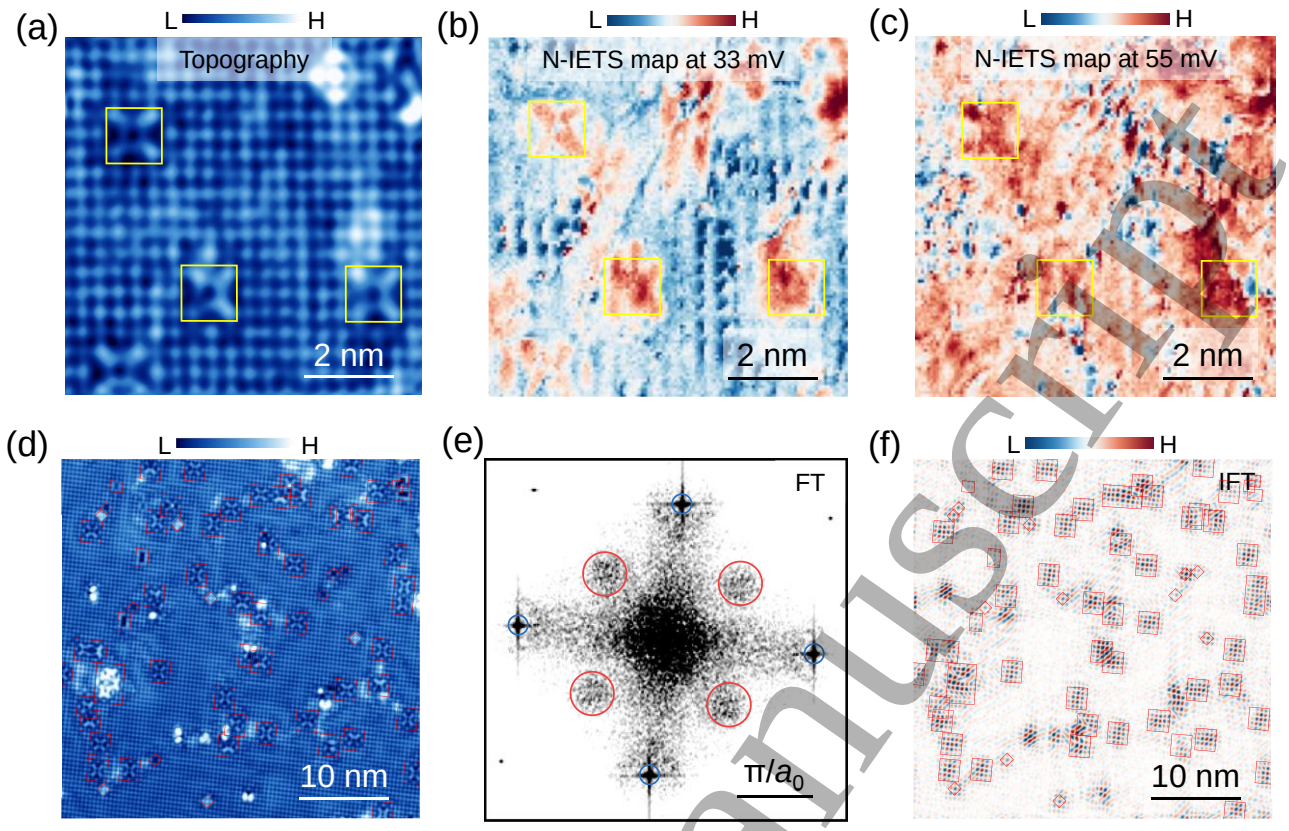

Fig. 4. Defect-pinned short-range $\sqrt{2}\times\sqrt{2}$ order and selective suppression of phonon modes. (a), STM topography (V_s =-120 mV, I_t =400 pA) of the B-terminated surface with defects. (b),(c), real-space normalized-IETS maps acquired at energies of 33 mV (b) and 55 mV (c), respectively. Yellow squares mark the defect sites and the associated short-range modulation. (d), large-area STM image (V_s =-120 mV, I_t =400 pA) of the B-terminated surface. (e), two-dimensional Fourier transform of (d). Blue circles indicate the Bragg peaks of the B-terminated surface, and red circles highlight a pronounced diffuse enhancement near the M points of q-space, corresponding to a $\sqrt{2}\times\sqrt{2}$ short-range order. (f), real-space map of the $\sqrt{2}\times\sqrt{2}$ order obtained by inverse Fourier transforming the red-circled region in (e). The red squares in (d) and (f) mark the defect sites and the associated short-range modulation, with a one-to-one correspondence between the two panels.

In summary, IETS on the B-terminated surface of EuB_6 obtained by low-temperature cleavage resolves a cascade of stable Inelastic channels at ~11, 31, 55, and 93 mV. Near defects, the LDOS around the E_F is elevated, whereas the energies of these Inelastic channels remain nearly unchanged and their intensities are redistributed in a mode-selective manner. This behavior indicates that defects modulate the local phonon excitation probability and electron-phonon coupling strength. Furthermore, Fourier

analysis of topography reveals a $\sqrt{2}\times\sqrt{2}$ short-range order in defect-proximal regions of the B-terminated surface. This defect-pinned lattice modulation selectively modifies the charge density and the local EPC strength on neighboring lattice sites. These results provide real-space insight into the interplay between surface phonons, defects, and low-energy electronic states in EuB_6.

References

[1] Cheong S-W and Mostovoy M 2007 *Nat. Mater.* **6** 13.

[2] Cui J, Boström E V, Ozerov M, Wu F, Jiang Q, Chu J-H, Li C, Liu F, Xu X, Rubio A and Zhang Q 2023 *Nat. Commun.* **14** 3396.

[3] Bao S, Gu Z-L, Shangguan Y, Huang Z, Liao J, Zhao X, Zhang B, Dong Z-Y, Wang W, Kajimoto R, Nakamura M, Fennell T, Yu S-L, Li J-X and Wen J 2023 *Nat. Commun.* **14** 6093.

[4] Zhang X, Zhang Y, Okamoto S and Xiao D 2019 *Phys. Rev. Lett.* **123** 167202.

[5] You S, Lü J-T, Guo J and Jiang Y 2017 *Advances in Physics: X* **2** 907.

[6] Calderón M, Wegener L and Littlewood P 2004 *Phys. Rev. B* **70** 092408.

[7] Snow C, Cooper S, Young D, Fisk Z, Comment A and Ansermet J-P 2001 *Phys. Rev. B* **64** 174412.

[8] Nyhus P, Yoon S, Kauffman M, Cooper S, Fisk Z and Sarrao J 1997 *Phys. Rev. B* **56** 2717.

[9] Süllow S, Prasad I, Bogdanovich S, Aronson M, Sarrao J and Fisk Z 2000 *J. Appl. Phys.* **87** 5591.

[10] Wirth S and Schlottmann P 2021 *Adv. Quantum Technol.* **4** 2100102.

[11] Gabani S, Flachbart K, Siemensmeyer K and Mori T 2020 *J. Alloy. Compd.* **821** 153201.

[12] Hong J, Mutalik S, Pescarmona P P and Protesescu L 2024 *Chem. Mater.* **36** 2147.

[13] Zabolotnyy V, Fürsich K, Green R, Lutz P, Treiber K, Min C-H, Dukhnenko A, Shitsevalova N, Filipov V and Kang B 2018 *Phys. Rev. B* **97** 205416.

[14] Coe A, Zhu Z-H, He Y, Kim D-J, Fisk Z, Hoffman J D and Hoffman J E 2025 *Phys. Rev. Lett.* **134** 236205.

[15] Wirth S, Rößler S, Jiao L, Ale Crivillero M V, Rosa P F and Fisk Z 2021 *Phys. Status Solidi B* **258** 2000022.

[16] Trenary M 2012 *Sci. Technol. Adv. Mater.* **13** 023002.

[17] Degiorgi L, Felder E, Ott H, Sarrao J and Fisk Z 1997 *Phys. Rev. Lett.* **79** 5134.

[18] Ogita N, Nagai S, Okamoto N, Udagawa M, Iga F, Sera M, Akimitsu J and Kunii S 2003 *Phys. Rev. B* **68** 224305.

[19] Broderick S, Ruzicka B, Degiorgi L, Ott H R, Sarrao J L and Fisk Z 2002 *Phys. Rev. B* **65** 121102.

[20] Zirngiebl E, Hillebrands B, Blumenröder S, Güntherodt G, Loewenhaupt M, Carpenter J M, Winzer K and Fisk Z 1984 *Phys. Rev. B* **30** 4052.

[21] Basov D N, Averitt R D, Van Der Marel D, Dressel M and Haule K 2011 *Rev. Mod. Phys.* **83** 471.

[22] Devereaux T P and Hackl R 2007 *Rev. Mod. Phys.* **79** 175.

[23] Kim J-H, Lee Y, Homes C, Rhyee J-S, Cho B K, Oh S-J and Choi E 2005 *Phys. Rev. B* **71** 075105.

[24] Shen J, Gao J, Yi C, Li M, Zhang S, Yang J, Wang B, Zhou M, Huang R and Wei H 2023 *Innovation* **4**.

[25] Fisk Z, Johnston D, Cornut B, Von Molnar S, Oseroff S and Calvo R 1979 *J. Appl. Phys.* **50** 1911.

[26] Kim J, Kim Y-J, Kuneš J, Cho B K and Choi E 2008 *Phys. Rev. B* **78** 165120.

[27] Kim J, Ku W, Lee C-C, Ellis D, Cho B, Said A, Shvyd'ko Y and Kim Y-J 2013 *Phys. Rev. B* **87** 155104.

[28] Pan L, Wang Y, Ding X, Hu G, Guo H, Lv S, Xian G, Qi Q, Zhu K, Han Y, Lei M, Li Z, Bao L, Zhang Y, Lin X, Zhu S, Peng R, Yang H and Gao H-J 2024 *Appl. Phys. Lett.* **125**.

[29] Zhu K, Qi Q, Xie Y, Pan L, Lv S, Hu G, Zhao Z, Xian G, Han Y, Bao L, Zhang Y, Lin X, Guo H, Yang H and Gao H-J 2025 *Chin. Phys. B* **34** 097308.

[30] Süllow S, Prasad I, Aronson M, Sarrao J, Fisk Z, Hristova D, Lacerda A, Hundley M, Vigliante A and Gibbs D 1998 *Phys. Rev. B* **57** 5860.

[31] Manna R S, Das P, de Souza M, Schnelle F, Lang M, Müller J, von Molnár S and Fisk Z 2014 *Phys. Rev. Lett.* **113** 067202.

[32] Martinho H, Rettori C, Dalpian G, Da Silva J, Fisk Z and Oseroff S 2009 *J. Phys.: Condens. Matter* **21** 456007.

[33] Noguera C 2000 *J. Phys.: Condens. Matter* **12** R367.

[34] Buchsteiner P, Harmsen L, Ciomaga Hatnean M, Balakrishnan G and Wenderoth M 2020 *Phys. Rev. B* **102**.

[35] Wu Z-B, Gao Z-Y, Chen X-Y, Xing Y-Q, Yang H, Li G, Ma R, Wang A, Yan J and Shen C 2018 *Rev. Sci. Instrum.* **89** 113705.

[36] Rößler S, Jiao L, Seiro S, Rosa P F, Fisk Z, Rößler U K and Wirth S 2020 *Phys. Rev. B* **101** 235421.

[37] Gao S-Y, Xu S, Li H, Yi C-J, Nie S-M, Rao Z-C, Wang H, Hu Q-X, Chen X-Z and Fan W-H 2021 *Phys. Rev. X* **11** 021016.

[38] Lambe J and Jaklevic R 1968 *Phys. Rev.* **165** 821.

[39] Ruan W, Ye C, Guo M, Chen F, Chen X, Zhang G-M and Wang Y 2014 *Phys. Rev. Lett.* **112** 136401.

[40] De La Torre B, Švec M, Foti G, Krejčí O, Hapala P, Garcia-Lekue A, Frederiksen T, Zbořil R,

Arnau A and Vázquez H 2017 *Phys. Rev. Lett.* **119** 166001.

[41] Kim Y, Hellmuth T J, Burkle M, Pauly F and Scheer E 2011 *ACS nano* **5** 4104.

[42] Okabayashi N, Paulsson M, Ueba H, Konda Y and Komeda T 2010 *Phys. Rev. Lett.* **104** 077801.

[43] Lorente N, Persson M, Lauhon L J and Ho W 2001 *Phys. Rev. Lett.* **86** 2593.

[44] Nguyen T H, Nguyen T M H, Kang B, Cho B, Han M, Choi H J, Kong M, Lee Y and Yang I S 2019 *J. Raman. Spectrosc.* **50** 1661.

[45] Buchsteiner P, Sohn F, Horstmann J, Voigt J, Ciomaga Hatnean M, Balakrishnan G, Ropers C, Blöchl P and Wenderoth M 2019 *Phys. Rev. B* **100** 205407.

Acknowledgments

The work is supported by the National Key Research and Development Projects of China (2024YFA1207702, 2022YFA1204100), National Natural Science Foundation of China (62488201), the CAS Project for Young Scientists in Basic Research (YSBR-003), and the Quantum Science and Technology-National Science and Technology Major Project (2021ZD0302700).